How, where and when do radial faults grow near salt diapirs?

Alexander J. Coleman[1], Christopher A.-L. Jackson[1], Oliver B. Duffy[2] and Maria A. Nikolinakou[2]

[1] *Basins Research Group (BRG), Department of Earth Science and Engineering, Imperial College, Prince Consort Road, London, SW7 2BP, UK.*

[2] *Bureau of Economic Geology, The University of Texas at Austin, University Station, Box X, Austin, TX 78713-7508, USA.*

*Corresponding author: a.coleman14@imperial.ac.uk

Keywords: Salt tectonics, Radial faults, halokinetic sequences, drape folding, diapirism

Abstract

We examine 3-D seismic reflection data from the Santos Basin, offshore Brazil to determine how, where and when do radial faults grow near a sub-circular salt diapir (stock). We show roof stretching alone cannot account for the large heights and lengths of the kilometre-scale radial faults, suggesting stock widening ('stem push'), a mechanism implied in numerical models but not yet documented in natural examples, played a pivotal role in radial fault formation. We suggest that, when a diapir is covered by a roof, radial faults form in its overburden due to roof stretching, extending no further than the limit of the drape folding. The roof may then be shouldered aside and the faults buried along the stock flanks, exposing these strata to stem push-related stresses that may then reactivate pre-existing or form new radial faults. Radial faults, irrespective of how they formed, may dip-link with or offset one-another as salt continues to rise. We suggest the causal

mechanism for radial fault formation will likely change as roof thickness varies during diapirism, with this reflecting the ratio between sedimentation rate and salt volumetric flux. Our findings are likely applicable to other diapirs, helping us not only to interpret the paleo-stress state of salt-bearing sedimentary basins, but also advancing our understanding of fracture distributions, potential fluid flow pathways, and reservoir compartmentalization around salt diapirs in basins where seismic reflection imaging is poor.

1. INTRODUCTION

Sub-circular salt diapirs or 'stocks' are ubiquitous in salt-bearing sedimentary basins, and are typically associated with complex fault networks in surrounding country rock. The most common fault networks comprise 'radial faults' (i.e. normal faults that extend radially from a stock into flanking strata). Radial faults may control the migration of crustal fluids (e.g. Davison et al., 2000a) and compartmentalise hydrocarbon reservoirs (e.g. Carruthers et al., 2013), and may provide a relatively high-fidelity record of the evolving near-salt stress conditions associated with salt diapirism (cf. Quintà et al., 2012; Nikolinakou et al., 2014; Maerten et al., 2016).

Despite being widespread, and geologically and economically important, the origin of radial faults remains unclear. Radial faults in the unpierced roofs above rising stocks are undoubtedly related to outer-arc extension during active rise, herein termed 'roof stretching' (Fig. 1A). Roof stretching-related radial faults may nucleate anywhere in, but not necessarily extend fully across, the arched overburden. As a stock pierces its overburden, roof radial faults may be eroded or shouldered aside, and buried along the stock flanks (e.g. Withjack and Scheiner, 1982; Yin and Groshong Jr, 2007; Carruthers et al., 2013). Stretching and shouldering of the roof may occur during 'drape folding' in passive diapirism (Giles and Rowan, 2012), or alternatively during active rise driven by regional shortening (Davison et al., 2000b; Dooley et al., 2009; Jackson and Hudec, 2017).

Radial faults may also form due to a widening stock pushing outwards against its flanking strata (e.g. Bishop, 1978; Fig. 7 in Nikolinakou et al., 2014), herein termed ‘stem push’ (Fig. 1B). Stem push-related radial faults form at the salt-sediment interface where circumferential stretching is greatest and where the horizontal stresses are anisotropic (i.e. $\sigma_H \neq \sigma_h$). Although numerical models suggest stem push is a plausible mechanism to form radial faults (e.g. Nikolinakou et al., 2014), this prediction has never been critically tested using observations from a natural salt diapir, nor have the associated strains been characterised and quantified.

Drape folding above a passively rising diapir is typically recorded by Composite Halokinetic Sequences (‘CHS’; Giles and Rowan, 2012), with two end-members recognised – tapered and tabular. Tapered CHS form when the salt is buried by a relatively thick roof, as sedimentation rate outpaces the volumetric flux of salt; in this case, broad, km-scale drape folds form. Tabular CHS form when the salt is at or very near the surface and covered by only a relatively thin roof i.e. the volumetric flux of salt is greater or equal to the sedimentation rate (e.g. Giles and Rowan, 2012; Jackson and Hudec, 2017); in this case, narrow drape folds (< 200 m) form next to the salt-sediment interface. As the diapiric roof is pierced, drape fold-related radial faults are eroded, being buried and only preserved along the flanks (Fig. 1A). In tapered CHS, radial faults are expected to extend greater distances (<1000 m) from the salt due to broader folding compared to tabular CHS (<200 m). It follows that radial faults extending more than a few hundred metres laterally in tabular CHS must have been influenced by stem push or shortening rather than roof stretching, although this has never been critically tested.

Here, we test the hypotheses above by identifying CHS and applying quantitative fault analysis around a salt stock imaged in 3-D seismic reflection data from the Santos Basin, offshore Brazil (Fig. 1C). Using this approach, we: (i) link the genetic mechanism of radial fault formation to modes of salt diapirism, and (ii) to the best of our knowledge, for the first time using a natural example, test the validity of the stem push model, using exceptionally well-imaged radial faults flanking and overlying a salt stock (Fig. 2). These data not only allow us to map radial fault-diapir relationships in three-dimensions and constrain their kinematics, but also investigate when, during diapirism, roof stretching and stem push may occur.

Insert Fig. 1

2. DATASET AND METHODS

We used 225 km^2 of a 850 km^2, Kirchhoff pre-stack time-migrated (PSTM), zero-phase processed, 3-D seismic dataset. Inline and crossline spacing are 14 m and 25 m, respectively. A frequency of c. 15–40 Hz and assumed average velocity of c. 2000 m/s (after Jackson et al., 2014) yield an estimated vertical resolution of c. 12 m at shallow depths, decreasing to c. 35 m towards the base of supra-salt minibasins (see Appendix 1 for details). All seismic data are displayed in milliseconds two-way time (ms TWT), but measurements are converted from time to depth using an interval velocity of 2000 m/s. We first mapped three seismic horizons (H1–H3) to constrain salt body geometry, and the 3-D distribution of throw on, and kinematics of, individual faults (Appendix 2). Quantitative fault analysis was not undertaken for H1 as throw was at the limit of seismic resolution (i.e. <25 m; Appendix 3). We then identified nine stratigraphic units adjacent to the stock, assigning them to the two end-member CHS styles of Giles and Rowan (2012) based on the width of folding and thinning, and the geometry (convergent or parallel) of the bounding unconformities. These CHS allowed us to interpret periods when the rising diapir was buried by a thick (tapered CHS) or thin (tabular CHS) roof (Fig. 2) (see Giles and Rowan, 2012, for recognition criteria). We then grouped the units into three packages based on CHS style, and whether the stock had pierced strata at the structural level of observation. Package A consists of tabular CHS, whereas B and C contain tapered CHS. Packages A and B have been pierced by the salt, whereas C has not. H1 lies in Package A, H2 at the boundary between A and B, and H3 in C.

Insert Fig. 2

3. GEOLOGICAL SETTING

The Santos Basin formed during Early Cretaceous rifting and initial opening of the South Atlantic, during which time a thick Aptian salt layer was deposited (Ariri Formation) (Mohriak et al., 2008; Contreras et al., 2010). Subsequent deposition of Albian (carbonate-dominated) and Cenomanian-Holocene (siliciclastic-dominated) rocks, in addition to thin-skinned gravity-driven extension, drove seaward salt flow and diapir growth (Demercian et al., 1993; Modica and Brush, 2004; Davison et al., 2012). We focus on a salt stock located (Fig. 1D) within the proximal, extensional domain (after Davison et al., 2012), in an area unlikely to have undergone Albian shortening. Like many salt structures in this area, the stock initiated as an extensional reactive diapir, before undergoing passive and active rise driven by sediment loading (Jackson et al., 2015). Here, we focus only on the latter stages of diapirism once the stock had developed, where CHS and radial faults formed.

4. SALT STOCK AND OVERBURDEN GEOMETRY, AND DIAPIRISM

The salt stock is expressed in seismic data as a package of chaotic, low-amplitude reflections. In cross-section, the stock is c. 4 km tall and has a ‘finger’ geometry, consisting of an up to c. 2.3 km wide, smooth head and stem, and a <6 km wide pedestal (Fig. 2). In plan-view, the stock is sub-circular at shallow depths (c. 2000 ms TWT) and ovate at greater depths (c. 4000 ms TWT), with its long axis trending NE. The presence of tabular CHS (with narrow drape folds <200 m from the salt) at deeper levels indicates that, following diapir initiation, the stock entered a protracted phase of passive diapirism where the volumetric flux of salt exceeded that of the background sedimentation (Package A). Tapered CHS (with broad drape folds <1000 m from the salt) dominate at shallower levels, suggesting sedimentation rate outpaced the volumetric flux of salt (packages B and C). This could reflect an increase in the regional sedimentation rate, or a decreased volumetric flux of salt as the source layer thinned and ultimately welded.

Shortening has been documented regionally in the Santos Basin (e.g. Demercian et al., 1993; Modica and Brush, 2004; Contreras et al., 2010). However, based on the location of the stock in the extensional domain (after Davison et al., 2012), the sub-circular map-view geometry (cf. Jackson and Hudec, 2017), a lack of concentric thrusts in the roof (cf. Withjack and Scheiner, 1982; Davison et al., 2000b), and the absence of a fault-bounded 'primary indentor' in the putative hinterland of the diapir (Dooley et al., 2009), we interpret diapir growth was *not* driven by shortening. If shortening has occurred, it must be cryptic (e.g. Davison et al., 2000a; Davison et al., 2000b).

5. RADIAL FAULTS

Geometry and Distribution

Radial faults are broadly linear in map view at all stratigraphic intervals (H1–3), although they vary in their distribution, density, and length (Fig. 3). They occur over a c. 2.5 km depth range (c. 1–3.5 km) within tapered and tabular CHS, although they tend to cluster around the stock head in tapered CHS (H2–3). It is possible that radial faults exist but are not imaged at greater depths (>3.5 km). Individual faults are planar, 400–1400 m tall, have aspect ratios of <2 (Appendix 4), dip at 50–60°, and have throws <80 m. Faults occur in vertically stacked tiers; faults within each tier have similar geometric characteristics e.g. heights, lengths and densities. Largely undeformed intervals define tier boundaries. Tall radial faults may cross-cut several tier boundaries and are best-developed at shallower levels around the head of the stock in packages B and C (Fig. 4; Appendix 5).

Insert Fig. 3

Throw Distribution

We study the distribution of throw on radial faults to determine where these structures nucleated with respect to the stock, which in turn, may reveal the mechanism responsible for their formation. Throw maxima for faults offsetting H2–3 occur immediately at or some distance from the salt-sediment interface (maximum 3 km from the stock centre; white squares on Fig. 3; Appendix 6). Faults typically have ‘C-type’ throw-depth profiles (*sensu* Muraoka and Kamata, 1983), with a throw maximum near their centres and very low gradients at their upper tips (<0.1) (Fig. 4A; Appendix 7). Some faults may have several throw maxima separated by throw minima, and may offset presumably older, neighbouring faults (Fig. 4B). Faults are not associated with growth strata (expansion indices of c. 1; Fig. 4), suggesting they were blind.

Insert Fig. 4

Kinematics and Origin

Based on their geometry, stratigraphic occurrence within tapered and tabular CHS, and throw distribution, we propose the radial faults have two origins. Radial faults developed in the diapir roof and contained in tapered CHS, with throw maxima (i.e. nucleation points; Muraoka and Kamata, 1983; Baudon and Cartwright, 2008) located both above and outboard of the stock, and which do not intersect the salt, formed only due to roof stretching (H3 in Fig. 3; Package C in Fig. 2).

In contrast, radial faults within tabular CHS, and which are in contact with and extend several kilometres from the salt-sediment interface, that is, well beyond the limit of drape folding, formed due to stem push (H1 in Fig. 3; Package A in Fig. 2). These faults nucleated at the salt-sediment interface where the circumferential extension is greatest (e.g. Nikolinakou et al., 2014; Jackson and Hudec, 2017). As the stock was at or near the surface with only a relatively thin roof during deposition of tabular CHS, radial faults associated with roof stretching would be limited to the relatively narrow extent of drape folding (<200 m), immediately adjacent to the stock. Roof stretching therefore cannot be responsible for the formation of radial faults now deeply buried in the stock flanks that extend kilometres away from the salt. Given the majority of deep radial faults are not physically connected to shallow radial faults associated with roof stretching (Appendix 5), they cannot be attributed to downward propagation of the shallower-level structures; they must therefore reflect a mechanism other than drape folding. Some radial faults grew to heights of several kilometres (Fig. 4), thus it is unlikely they could form due to roof stretching alone, as passive diapirs driven cannot arch km-thick roofs (e.g. Davison et al., 2000b; Jackson and Hudec, 2017). Furthermore, given the lack of evidence for regional shortening, a mechanism that could have lifted km-thick diapir roofs and generated km-tall faults, we propose such tall faults likely grew due to stem push during passive diapirism (Nikolinakou et al., 2014).

Having considered radial faults in tabular CHS, we now explore which mechanism likely produced radial faults in Package B (pierced tapered CHS). Radial faults in Package B have their throw maxima either outboard of the salt or at the salt-sediment interface (H2 in Fig. 3). The former suggests roof stretching must have occurred over a broad region with discontinuous faulting; however, the latter could feasibly be explained by either: (i) stem push, or (ii) roof stretching, and subsequent diapiric piercement of the overburden. In the first case, radial faults nucleate where circumferential extension is greatest, due to stem push at the salt-sediment interface (Fig. 1B). In the second case, piercement of the overburden removes sections of the roof, and portions of radial faults formed by roof stretching, thus truncating the original throw distribution. Throw maxima could therefore be only coincidentally located at the salt-sediment interface. Because the radial faults were blind and were not associated with growth strata, we are unable to identify whether stem push may have reactivated pre-existing roof stretching faults as the strata became buried (e.g. Package B). Irrespective of the mechanism driving their formation, radial faults grew, dip-linked, and/or offset pre-existing radial faults beside the stock (Fig. 4B) (cf. Muraoka and Kamata, 1983; Baudon and Cartwright, 2008).

6. DISCUSSION AND IMPLICATIONS

Numerical (e.g. Yin and Groshong Jr, 2007) and physical (e.g. Parker and McDowell, 1951; Withjack and Scheiner, 1982) models, maps of mined salt stocks (e.g. Barton, 1925) and exposed diapirs (e.g. Powers and Hopkins, 1922; Quintà et al., 2012), and seismic reflection data (e.g. Davison et al., 2000a; Stewart, 2006; Carruthers et al., 2013) provided a largely 2-D understanding of radial fault geometry and growth. However, by undertaking detailed mapping of 3-D seismic reflection data, we are able to not only better determine the full, 3-D geometry of *in-situ* radial fault networks, but to also constrain their kinematics. Based on our observations from the Santos Basin, we propose a genetic model that may be broadly applicable to other diapirs (e.g. the North Sea - Davison et al., 2000; Basque-Pyrenees – Quinta et al., 2012; US Gulf Coast – Parker and McDowell, 1951). We propose that, as a salt stock grows and roof thickness varies with changes in the volumetric flux of salt and/or sedimentation rate, it is likely the mechanism responsible for forming radial faults will vary. Such changes in the relative balance salt flux and sedimentation rate may, for example, reflect progressive welding of supra-salt minibasins and/or changes in regional sedimentation rate.

Once passive diapirism occurs and a stock starts to grow, the volumetric flux of salt may outpace the background sedimentation rate, meaning the stock will be at or near the depositional surface, covered only by a relatively thin roof (i.e. tabular CHS). As this thin roof is arched and is shouldered aside by the rising diapir, roof stretching-related radial faults will be buried and preserved immediate adjacent to (<200 m) the salt-sediment interface. As the source layer thins and the volumetric flux of salt decreases, the stock may be buried by a relatively thick roof (i.e. tapered CHS). Subsequent rise of the diapir generates stretching-related radial faults in the aggrading overburden, over a relatively broad area (<1000 m). Shouldering aside and burial of the roof along the flanks (regardless of the CHS type) may expose these strata to stem push-related stresses, reactivating pre-existing or forming new radial faults. Faults in the vicinity of the salt may continue to grow throughout diapirism, becoming taller and propagating laterally. Stem push-related reactivation of old faults, and the formation of new faults, will be likely concentrated towards the upper parts of stocks where the greatest stress perturbations occur (e.g. Fig. 8-9 in Nikolinakou et al., 2014). Finally, as the salt supply is exhausted and minibasins weld, sedimentation rate may outpace the volumetric flux of salt, causing stock burial (cf. Giles and Rowan, 2012; Jackson and Hudec, 2017). Once diapirism ceases, no further radial faults form unless latter extension or shortening occurs.

As the genetic mechanism for forming radial faults likely changes during diapirism, the geometry and kinematics of those faults will likely change, especially where they have interacted to create complex fault geometries. This could prove problematic when inverting fault network geometry for paleo-stress conditions (cf. Quintà et al., 2012; Carruthers et al., 2013; Maerten et al., 2016), leading to false interpretations of stress conditions, and the mode and distribution of fractures around salt stocks. In addition, we highlight the structural variability and potential reservoir compartmentalisation that may occur around salt stocks, providing insights into areas where radial faults are not exposed or are poorly imaged (e.g. Jones and Davison, 2014).

ACKNOWLEDGMENTS

We thank Investigação Petrolífera Limitada (PGS) for the provision of and permission to publish seismic, Schlumberger for the provision of the Petrel software licenses to Imperial College London. Michael R. Hudec, Mark G. Rowan, Thilo Wrona, and Tim P. Dooley are thanked for their discussions regarding passive diapirism, drape folding and faulting. Katherine Giles, Ian Davison, and Stefano Tavani are thanked for their comprehensive reviews that substantially improved this manuscript.

REFERENCES

Barton, D. C., 1925, The American salt-dome problems in the light of the Roumanian and German salt domes: AAPG Bulletin, v. 9, no. 9, p. 1227-1268.

Baudon, C., and Cartwright, J. A., 2008, 3D seismic characterisation of an array of blind normal faults in the Levant Basin, Eastern Mediterranean: Journal of Structural Geology, v. 30, no. 6, p. 746-760.

Carruthers, D., Cartwright, J., Jackson, M. P. A., and Schutjens, P., 2013, Origin and timing of layer-bound radial faulting around North Sea salt stocks: New insights into the evolving stress state around rising diapirs: Marine and Petroleum Geology, v. 48, p. 130-148.

Contreras, J., Zühlke, R., Bowman, S., and Bechstädt, T., 2010, Seismic stratigraphy and subsidence analysis of the southern Brazilian margin (Campos, Santos and Pelotas basins): Marine and Petroleum Geology, v. 27, no. 9, p. 1952-1980.

Davison, I., Alsop, G. I., Evans, N. G., and Safaricz, M., 2000a, Overburden deformation patterns and mechanisms of salt diapir penetration in the Central Graben, North Sea: Marine and Petroleum Geology, v. 17, no. 5, p. 601-618.

Davison, I., Alsop, I., Birch, P., Elders, C., Evans, N., Nicholson, H., Rorison, P., Wade, D., Woodward, J., and Young, M., 2000b, Geometry and late-stage structural evolution of Central Graben salt diapirs, North Sea: Marine and Petroleum Geology, v. 17, no. 4, p. 499-522.

Davison, I., Anderson, L., and Nuttall, P., 2012, Salt deposition, loading and gravity drainage in the Campos and Santos salt basins: Geological Society, London, Special Publications, v. 363, no. 1, p. 159-174.

Demercian, S., Szatmari, P., and Cobbold, P. R., 1993, Style and pattern of salt diapirs due to thin-skinned gravitational gliding, Campos and Santos basins, offshore Brazil: Tectonophysics, v. 228, no. 3, p. 393-433.

Dooley, T. P., Jackson, M. P., and Hudec, M. R., 2009, Inflation and deflation of deeply buried salt stocks during lateral shortening: Journal of Structural Geology, v. 31, no. 6, p. 582-600.

Giles, K. A., and Rowan, M. G., 2012, Concepts in halokinetic-sequence deformation and stratigraphy: Geological Society, London, Special Publications, v. 363, no. 1, p. 7-31.

Jackson, C. A.-L., Jackson, M. P., and Hudec, M. R., 2015, Understanding the kinematics of salt-bearing passive margins: A critical test of competing hypotheses for the origin of the Albian Gap, Santos Basin, offshore Brazil: Geological Society of America Bulletin, v. 127, no. 11-12, p. 1730-1751.

Jackson, C. A.-L., Jackson, M. P. A., Hudec, M. R., and Rodriguez, C., 2014, Internal structure, kinematics, and growth of a salt wall: Insights from 3-D seismic data: Geology, v. 42, no. 4, p. 307-310.

Jackson, M. P., and Hudec, M. R., 2017, Salt Tectonics: Principles and Practice, Cambridge University Press.

Jones, I. F., and Davison, I., 2014, Seismic imaging in and around salt bodies: Interpretation, v. 2, no. 4, p. SL1-SL20.

Maerten, L., Maerten, F., Lejri, M., and Gillespie, P., 2016, Geomechanical paleostress inversion using fracture data: Journal of Structural Geology, v. 89, p. 197-213.

Modica, C. J., and Brush, E. R., 2004, Postrift sequence stratigraphy, paleogeography, and fill history of the deep-water Santos Basin, offshore southeast Brazil: AAPG bulletin, v. 88, no. 7, p. 923-945.

Mohriak, W., Nemčok, M., and Enciso, G., 2008, South Atlantic divergent margin evolution: rift-border uplift and salt tectonics in the basins of SE Brazil: Geological Society, London, Special Publications, v. 294, no. 1, p. 365-398.

Muraoka, H., and Kamata, H., 1983, Displacement distribution along minor fault traces: Journal of Structural Geology, v. 5, no. 5, p. 483-495.

Nikolinakou, M. A., Flemings, P. B., and Hudec, M. R., 2014, Modeling stress evolution around a rising salt diapir: Marine and Petroleum Geology, v. 51, p. 230-238.

Parker, T. J., and McDowell, A. N., 1951, Scale models as guide to interpretation of salt-dome faulting: Geological notes: AAPG Bulletin, v. 35, no. 9, p. 2076-2086.

Powers, S., and Hopkins, O. B., 1922, The Brooks, Steen, and Grand Saline Salt Domes Smith and Van Zandt Counties, Texas: Washington: Government Printing Office.

Quintà, A., Tavani, S., and Roca, E., 2012, Fracture pattern analysis as a tool for constraining the interaction between regional and diapir-related stress fields: Poza de la Sal Diapir (Basque Pyrenees, Spain): Geological Society, London, Special Publications, v. 363, no. 1, p. 521-532.

Stewart, S. A., 2006, Implications of passive salt diapir kinematics for reservoir segmentation by radial and concentric faults: Marine and Petroleum Geology, v. 23, no. 8, p. 843-853.

Withjack, M. O., and Scheiner, C., 1982, Fault patterns associated with domes--an experimental and analytical study: AAPG Bulletin, v. 66, no. 3, p. 302-316.

Yin, H., and Groshong Jr, R. H., 2007, A three-dimensional kinematic model for the deformation above an active diapir: AAPG bulletin, v. 91, no. 3, p. 343-363.

FIGURE CAPTIONS

Fig. 1 – Formation of radial faults via roof stretching (A) and stem push (B) with idealised fault throw-length plots. Radial fault Y throw increases towards the salt until it comes in contact with the salt. Radial fault X does not come in contact with the salt. Geographic context and variance slice at 1500 ms TWT showing the 3-D seismic extent (C). (column width figure)

Fig. 2 – Seismic section showing the salt stock and stratigraphic position of H1–3 and packages A–C. Interpreted tapered CHS – red, and tabular CHS – blue, are also shown. CHS may exhibit different degrees of upturn next to the salt, forming cusps (inset). For location, see Fig. 1C. Vertical exaggeration ~ 5. Seismic attribute is envelope. (column width figure)

Fig. 3 – Variance attribute map for H1–3, delineating radial faults and the salt. Throw maxima (white squares) for individual radial faults, throw-length plots for radial faults 1 and 2, and the position of Fig. 4 are also shown. For location, see Fig. 1B. Throw maxima are absent for H1 as measured throw is at the limit of seismic resolution. (two column width figure)

Fig. 4 – Radial fault 3 and 4 throw-depth profiles (solid line) and expansion indices (dashed line). White circles and squares show the vertical fault tips and throw maxima, respectively. Radial fault 3 has a simple throw-depth profile with a single throw maximum (A). Radial fault 2 shows cross-cutting of older faults (B) and two throw maxima indicative of dip linkage. Vertical exaggeration ~ 5. See Fig. 3 for the location. (two column width figure)

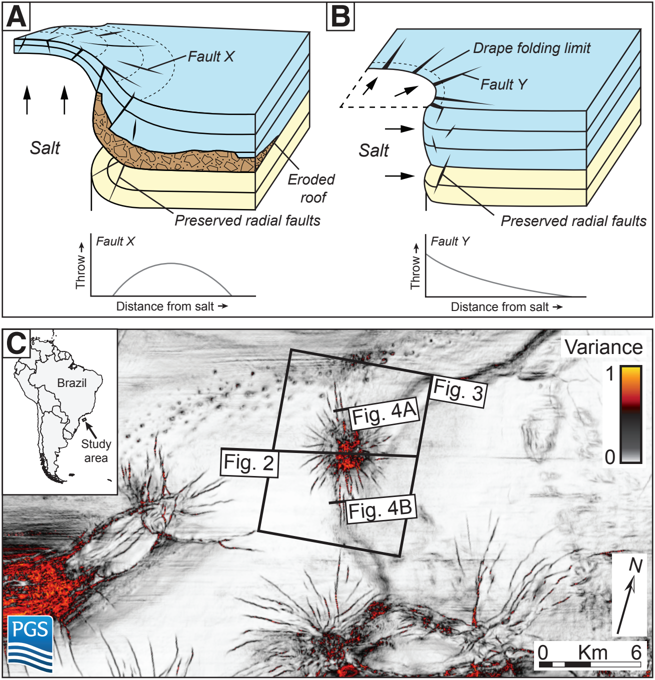
A
Fault X
Salt
Eroded roof
Preserved radial faults
Fault X
Throw
Distance from salt
B
Drape folding limit
Fault Y
Salt
Preserved radial faults
Fault Y
Throw
Distance from salt
C
Brazil
Study area
Variance
1
0
Fig. 3
Fig. 4A
Fig. 2
Fig. 4B
N
PGS
0 Km 6

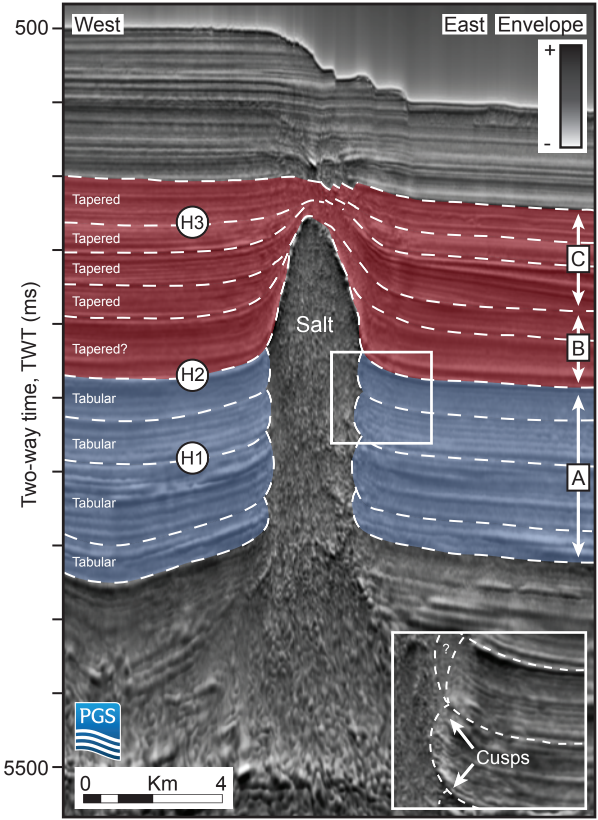

500
5500
Two-way time, TWT (ms)
West
East
Envelope
+
-
Tapered
H3
Tapered
Tapered
Tapered
Tapered?
H2
Tabular
Tabular
H1
Tabular
Tabular
Salt
C
B
A
?
Cusps
PGS
0
Km
4

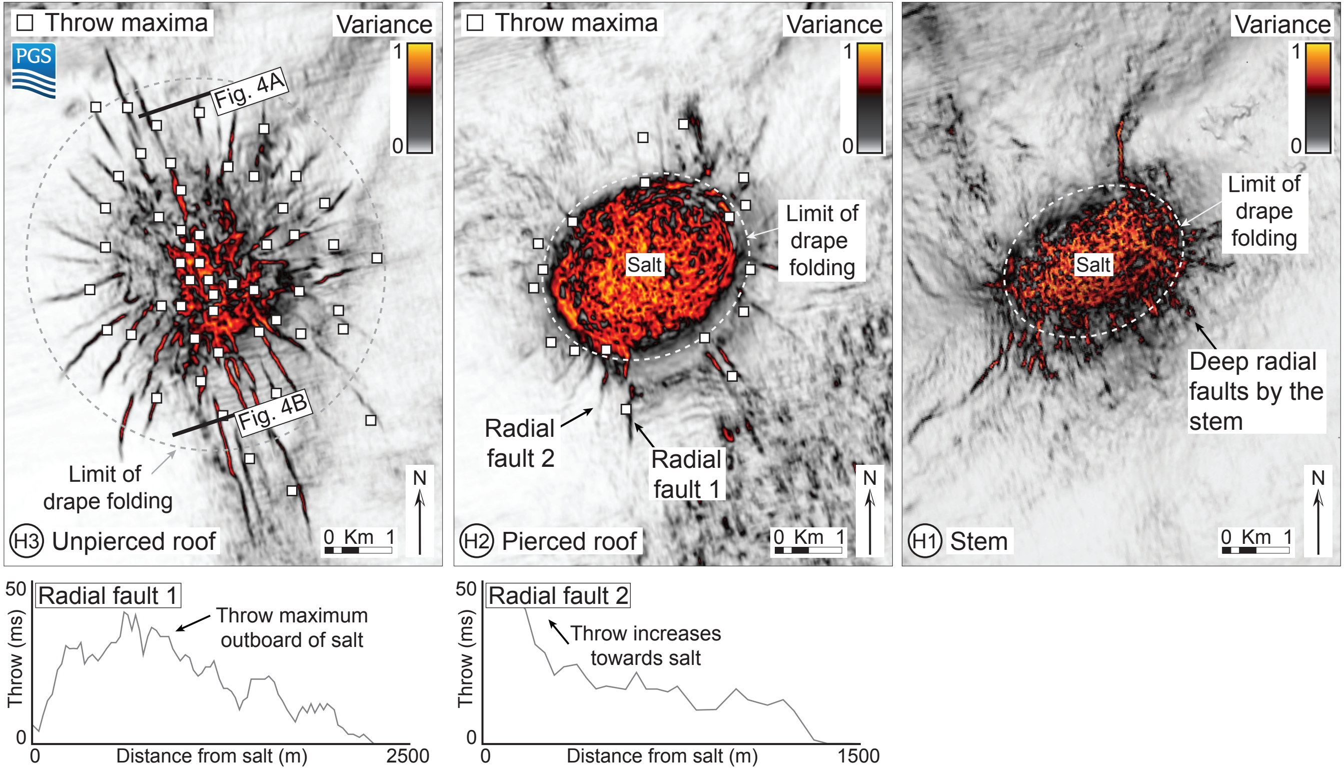

Throw maxima
Variance
1
0
PGS
Fig. 4A
Fig. 4B
Limit of drape folding
H3 Unpierced roof
0 Km 1
N
Throw maxima
Variance
1
0
Salt
Limit of drape folding
Radial fault 2
Radial fault 1
H2 Pierced roof
0 Km 1
N
Variance
1
0
Limit of drape folding
Salt
Deep radial faults by the stem
H1 Stem
0 Km 1
N
50
Radial fault 1
Throw maximum outboard of salt
Throw (ms)
0
0
Distance from salt (m)
2500
50
Radial fault 2
Throw increases towards salt
Throw (ms)
0
0
Distance from salt (m)
1500

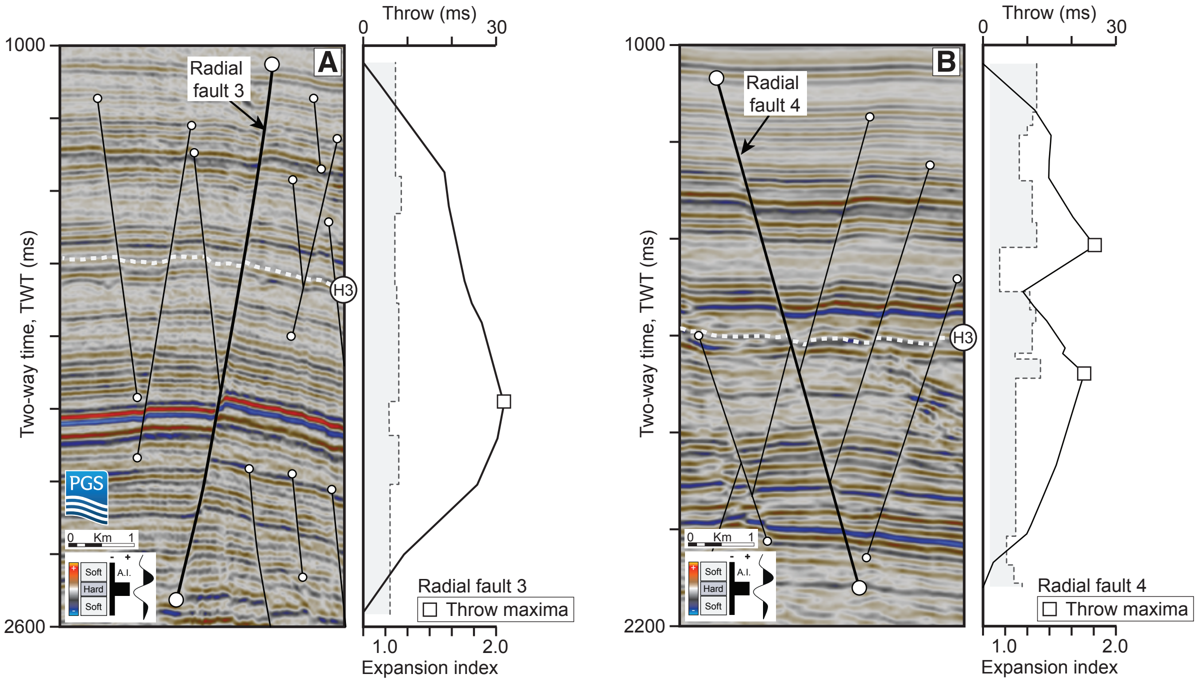

A
Radial fault 3
H3
PGS
0 Km 1
Soft
Hard
Soft
A.I.
Two-way time, TWT (ms)
1000
2600
Throw (ms)
0
30
1.0
2.0
Expansion index
Radial fault 3
Throw maxima
B
Radial fault 4
H3
0 Km 1
Soft
Hard
Soft
A.I.
Two-way time, TWT (ms)
1000
2200
Throw (ms)
0
30
1.0
2.0
Expansion index
Radial fault 4
Throw maxima

APPENDIX 1. AVERAGE VERTICAL SEISMIC RESOLUTION

Average vertical seismic resolution (red solid line) with depth using a velocity of ~ 2 km/s (after Jackson et al., 2014) and the frequency (black dashed line). The average vertical seismic resolution was calculated using the frequency and velocity. The instantaneous frequency is shown (left). Vertical exaggeration ~ 4.5.

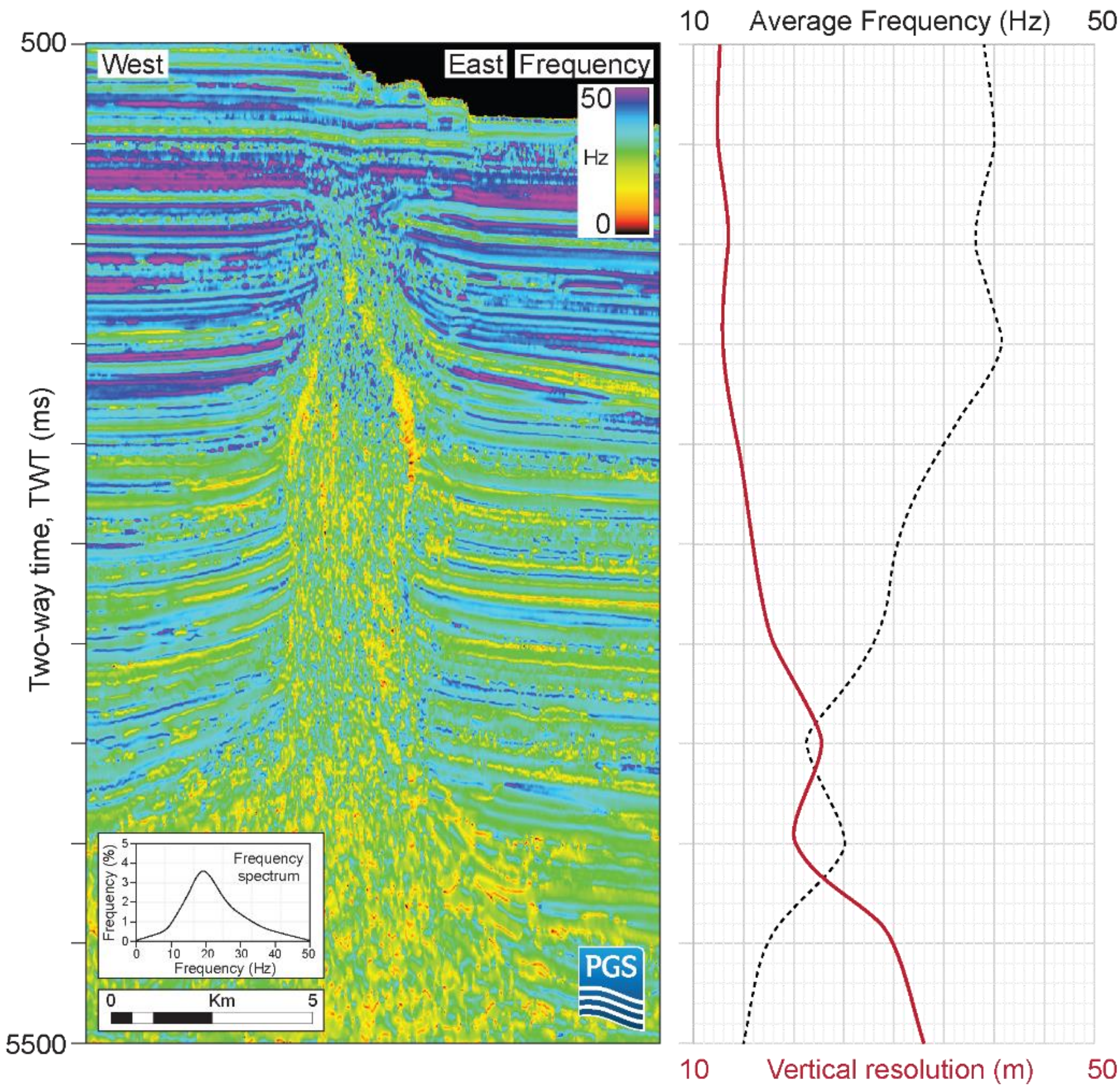

APPENDIX 2. QUANTITATIVE THROW ANALYSIS METHOD

Fault throw was measured perpendicular to radial fault strike every c. 50 – 100 m along the length of individual radial faults using horizon cut-offs (e.g. Muraoka and Kamata, 1983; Baudon and Cartwright, 2008). Cut-offs were defined using an extrapolated line that follows the regional trend of the chosen horizon prior to folding (Wilson et al., 2013), removing the effect of fault-parallel folding (Walsh et al., 1996). Therefore, total strain across the fault is accommodated, whether accommodated by ductile (continuous) or brittle (discontinuous) deformation (e.g. Long and Imber, 2010). The throw maxima was then identified on each radial fault, and plotted as white squares on Fig. 3. Fault throw was also measured with depth (T-z plots) using the aforementioned cut-offs, and throw maxima marked by white squares on Fig. 4.

Expansion indices illustrate variations in sediment thickness adjacent to fault systems, revealing the kinematics of bounding faults (e.g. Thorsen, 1963; Tvedt et al., 2013; Jackson et al., 2017). Expansion indices were calculated by dividing the hangingwall thickness of a stratal units by its corresponding footwall thickness and plotting these against geological time. An expansion index of 1 suggests no across-fault thickening, and a lack of syndepositional fault activity. An index of >1 suggests across-fault thickening and syndepositional fault activity. An index of <1 suggests stratal thinning from the footwall to the hangingwall, and may reflect difficulties in accurately measuring stratal thicknesses adjacent to a fault. Expansion indices near vertical fault tips may be slightly above and below one (± 0.1) due to ductile deformation (e.g. Barnett et al., 1987). T1 – T4 represent horizon tops. The white circle represents the vertical fault tip.

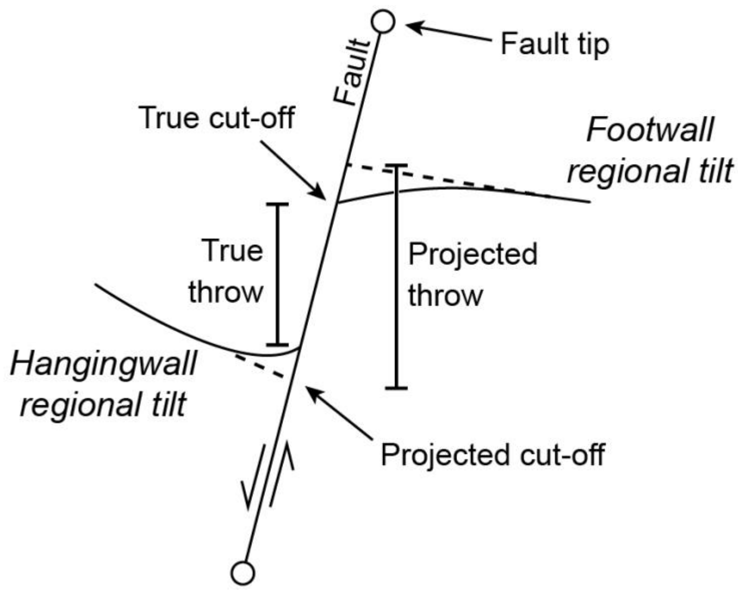
Fault tip
Fault
True cut-off
Footwall
regional tilt
True
throw
Projected
throw
Hangingwall
regional tilt
Projected cut-off

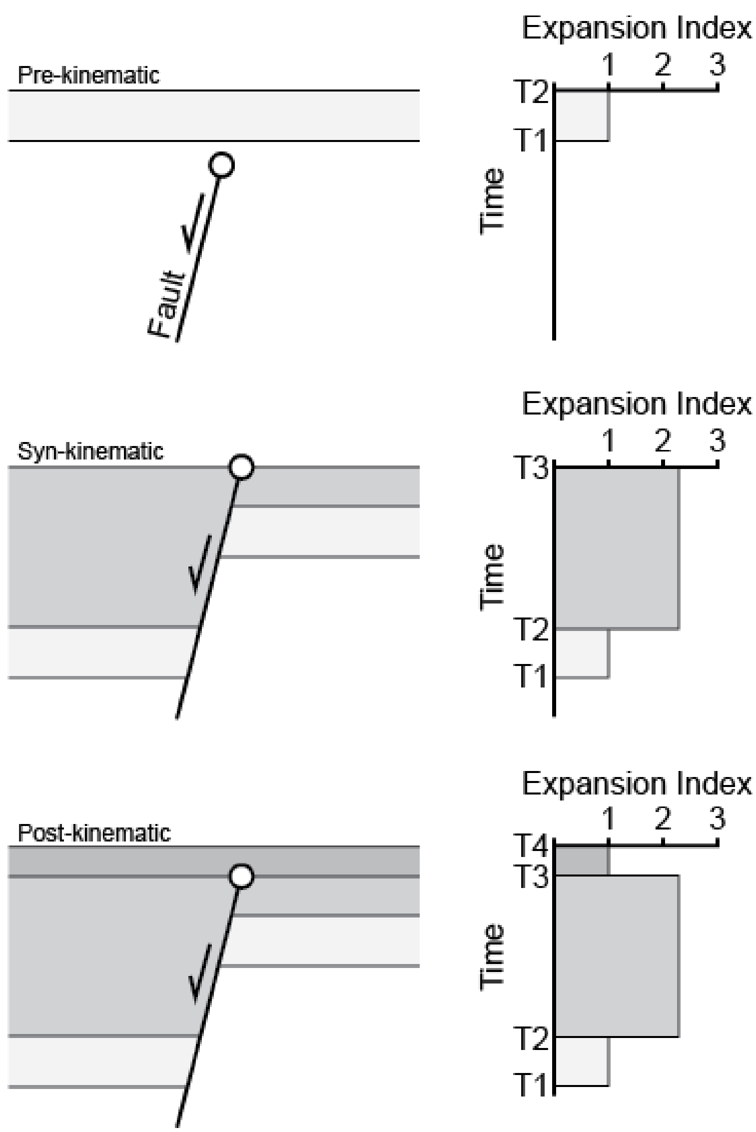
Pre-kinematic
Fault
Expansion Index
1 2 3
T2
T1
Time
Syn-kinematic
Expansion Index
1 2 3
T3
T2
T1
Time
Post-kinematic
Expansion Index
1 2 3
T4
T3
T2
T1
Time

References for Appendix 2

Barnett, J. A., Mortimer, J., Rippon, J. H., Walsh, J. J., and Watterson, J., 1987, Displacement geometry in the volume containing a single normal fault: AAPG Bulletin, v. 71, no. 8, p. 925-937.

Baudon, C., and Cartwright, J. A., 2008, 3D seismic characterisation of an array of blind normal faults in the Levant Basin, Eastern Mediterranean: Journal of Structural Geology, v. 30, no. 6, p. 746-760.

Jackson, C. A.-L., Bell, R. E., Rotevatn, A., and Tvedt, A. B. M., 2017, Techniques to determine the kinematics of synsedimentary normal faults and implications for fault growth models: Geological Society, London, Special Publications, v. 439.

Long, J., and Imber, J., 2010, Geometrically coherent continuous deformation in the volume surrounding a seismically imaged normal fault-array: Journal of Structural Geology, v. 32, no. 2, p. 222-234.

Muraoka, H., and Kamata, H., 1983, Displacement distribution along minor fault traces: Journal of Structural Geology, v. 5, no. 5, p. 483-495.

Thorsen, C. E., 1963, Age of growth faulting in southeast Louisiana.

Tvedt, A. B. M., Rotevatn, A., Jackson, C. A. L., Fossen, H., and Gawthorpe, R. L., 2013, Growth of normal faults in multilayer sequences: A 3D seismic case study from the Egersund Basin, Norwegian North Sea: Journal of Structural Geology, v. 55, p. 1-20.

Walsh, J. J., Watterson, J., Childs, C., and Nicol, A., 1996, Ductile strain effects in the analysis of seismic interpretations of normal fault systems: Geological Society, London, Special Publications, v. 99, no. 1, p. 27-40.

Wilson, P., Elliott, G. M., Gawthorpe, R. L., Jackson, C. A.-L., Michelsen, L., and Sharp, I. R., 2013, Geometry and segmentation of an evaporite-detached normal fault array: 3D seismic analysis of the southern Bremstein Fault Complex, offshore mid-Norway: Journal of Structural Geology, v. 51, p. 74-91.

APPENDIX 3. FAULT THROW RESOLUTION

Fault throw resolution for an example radial fault at Santos. Although vertical resolution may decrease with depth, the vertical offset between amplitude peaks between adjacent seismic traces permits fault throw to be measured to c. 5ms at shallow depths (< 3000 ms TWT). However, at greater depths (>3000 ms TWT), the peaks of individual traces become increasingly smeared as the vertical resolution decreases, and as such, vertical offsets are less distinct and measurement becomes increasingly difficult.

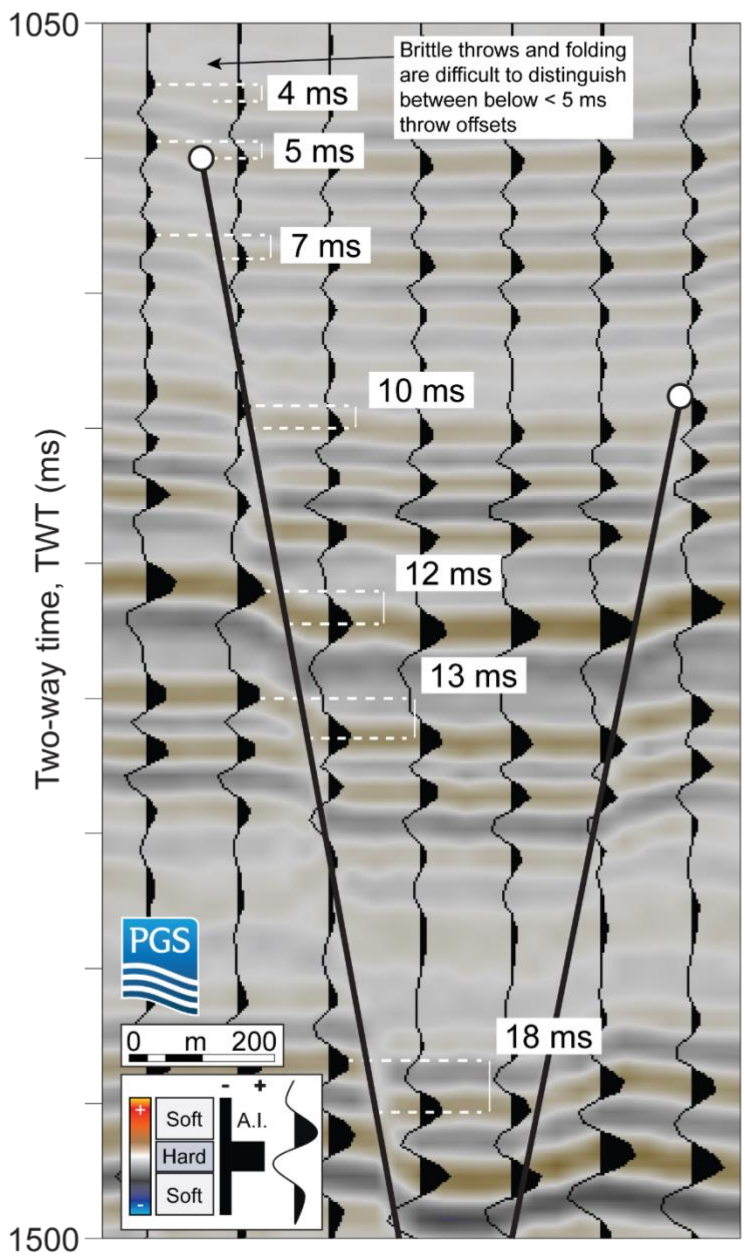

APPENDIX 4. ASPECT RATIO FOR SANTOS BASIN RADIAL FAULTS

Aspect ratios for Santos Basin radial faults. Velocity ~ 2km/s after Jackson et al. (2014).

Fault #	Max Length (m)	Height (m)	Aspect Ratio
1	3727	871	4.28
2	704	596	1.18
3	639	639	0.69
4	2021	811	2.49
5	1340	809	1.66
6	1131	655	1.73
7	601	361	1.66
8	2909	1521	1.91
9	1075	434	2.48
10	1732	650	2.66
11	644	557	1.16
12	1536	923	1.66
13	833	833	0.72
14	1542	620	2.49
15	1826	683	2.67
16	1100	208	5.29
17	1742	666	2.62
18	1322	500	2.64
19	2001	736	2.72
20	809	545	1.48
21	579	579	0.78
22	1246	275	4.53
23	1969	501	3.93
24	947	323	2.93
25	2585	676	3.82
26	882	735	1.20
27	1726	669	2.58
28	1490	731	2.04
29	1713	368	4.65
30	600	580	1.03
31	1146	663	1.73
32	644	579	1.11
33	1471	782	1.88
34	1004	350	2.87
35	412	412	0.90
36	754	496	1.52
37	903	670	1.35
38	2510	401	6.26
39	1457	693	2.10
40	464	464	0.82
41	726	726	0.52

42	540	540	0.92
43	955	685	1.39
44	856	657	1.30
45	1328	493	2.69
46	1072	734	1.46
47	791	726	1.09
48	1619	566	2.86
49	1580	551	2.87
50	1276	707	1.80
51	1288	463	2.78
52	859	701	1.23
53	1764	699	2.52
54	1090	480	2.27
55	964	596	1.62
56	754	754	0.88

APPENDIX 5. CIRCUMFERENTIAL SEISMIC SECTIONS

Circumferential seismic sections parallel to the salt-sediment interface documenting the different vertical tiers of radial faults around the isolated salt stock. H1 – 3 and Faults 1 - 4 are also shown.

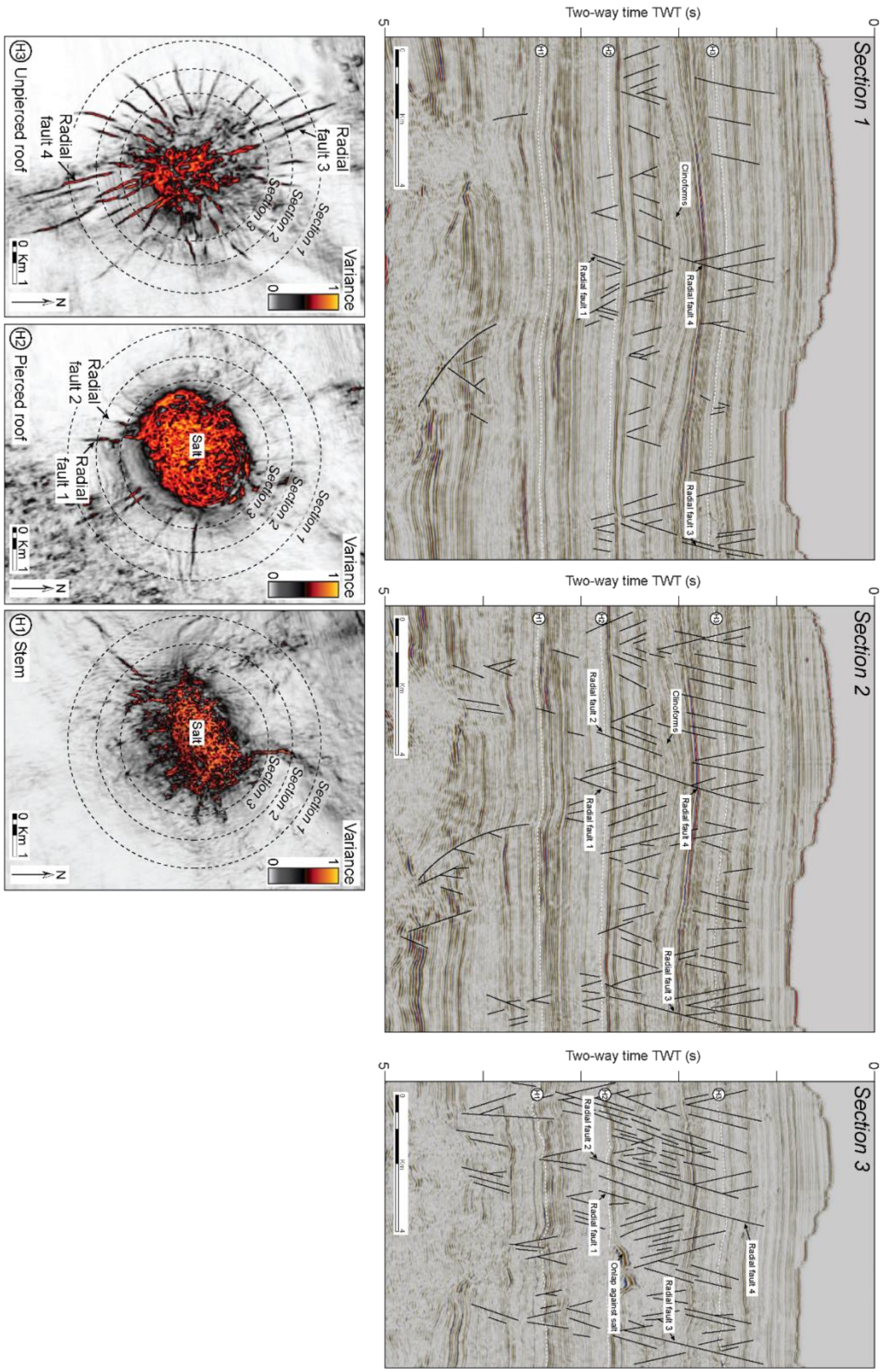

APPENDIX 6. RADIAL FAULT THROW FOR H2-3

Throw-distance on Fig. 3 used to determine the position of throw maxima along-strike for H2 - 3. Radial fault throw (i.e. strain) generally increases towards the diapir in H1 and H2.

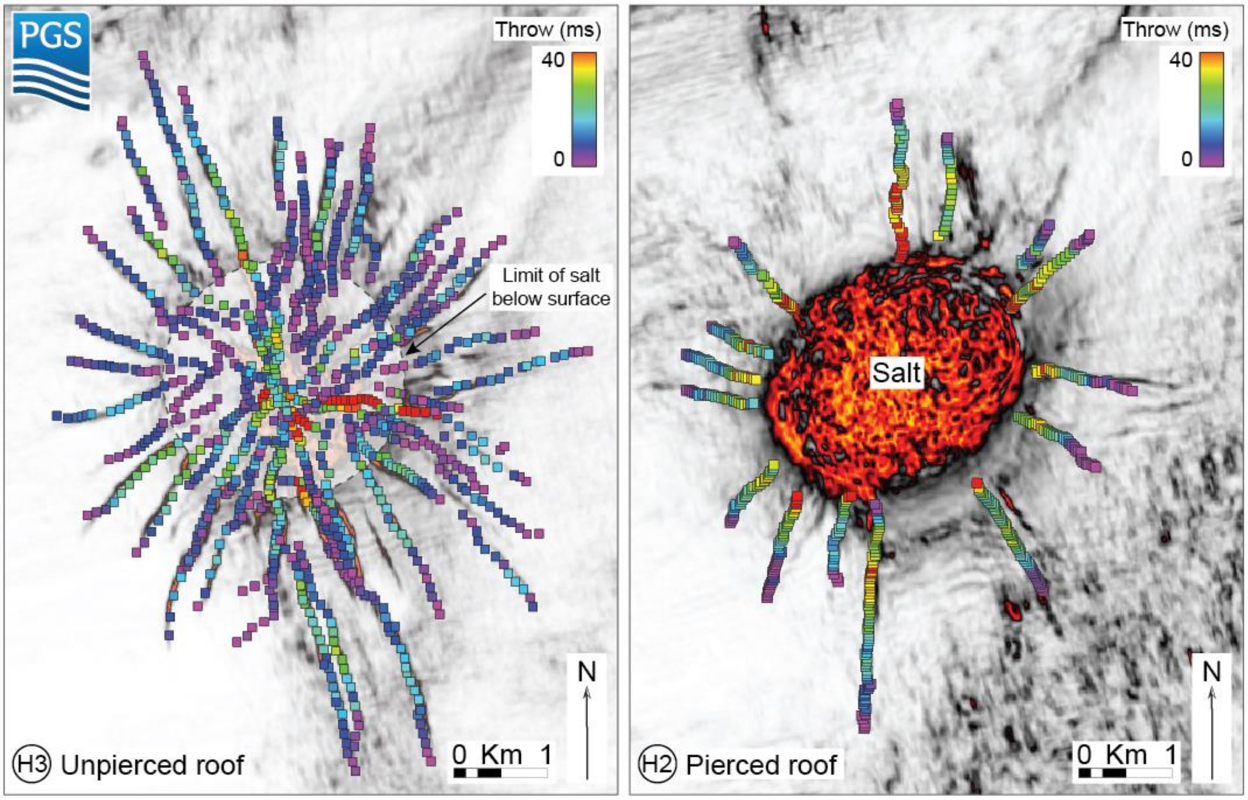

APPENDIX 7. UPPER THROW TIP GRADIENTS

Upper throw tip gradients for the Santos Basin radial faults.

Fault	Throw (m)	Upper tip radius (m)	Vertical tip throw gradient
1	47	494	0.09
2	32	308	0.10
3	25	350	0.07
4	25	281	0.09
5	25	202	0.12
6	20	139	0.14
7	26	197	0.13
8	23	499	0.05
9	23	233	0.10
10	21	303	0.07
11	36	322	0.11
12	37	507	0.07
13	21	123	0.17
14	16	151	0.11
15	15	66	0.23
16	29	254	0.11
17	38	368	0.10
18	30	307	0.10
19	24	126	0.19
20	20	338	0.06
21	20	147	0.14
22	20	305	0.07
23	20	469	0.04
24	20	454	0.04

25	66	515	0.13
26	60	499	0.12
27	22	125	0.18
28	22	206	0.11
29	23	310	0.07
30	22	427	0.05
31	21	312	0.07
32	19	231	0.08
33	19	194	0.10
34	22	396	0.06
35	24	250	0.09
36	21	335	0.06
37	14	284	0.05
38	18	247	0.07
39	21	248	0.08
40	18	337	0.05